

Optimizing the growth conditions of Al mirrors for superconducting nanowire single-photon detectors

Rasmus Flaschmann^{1,2,5,+,*}, Christian Schmid^{1,2,5,+}, Lucio Zugliani^{1,2,5}, Stefan Strothauer^{1,3,5}, Fabian Wietschorke^{1,2,5}, Stefanie Grotowski^{1,3,5}, Björn Jonas^{1,2,5}, Manuel Müller^{3,4}, Matthias Althammer^{3,4,5}, Rudolf Gross^{3,4,5}, Jonathan J. Finley^{1,3,5}, and Kai Müller^{1,2,5}

¹Walter Schottky Institut, Technical University of Munich, Germany

²Technical University of Munich, Germany; TUM School of School of Computation, Information and Technology, Department of Electrical Engineering

³Technical University of Munich, Germany; TUM School of School of Natural Sciences, Department of Physics

⁴Walther-Meißner-Institut, Bayerische Akademie der Wissenschaften, Germany

⁵Munich Center for Quantum Science and Technology (MCQST), Germany

*rasmus.flaschmann@wsi.tum.de

+these authors contributed equally to this work

ABSTRACT

We investigate the growth conditions for thin (≤ 200 nm) sputtered aluminum (Al) films. These coatings are needed for various applications, e.g. for advanced manufacturing processes in the aerospace industry or for nanostructures for quantum devices. Obtaining high-quality films, with low roughness, requires precise optimization of the deposition process. To this end, we tune various sputtering parameters such as the deposition rate, temperature and power, which enables 50 nm thin films with a root mean square (RMS) roughness of less than 1 nm and high reflectivity. Finally, we confirm the high-quality of the deposited films by realizing superconducting single-photon detectors integrated into multi-layer heterostructures consisting of an aluminum mirror and a silicon dioxide dielectric spacer. We achieve an improvement in detection efficiency at 780 nm from 40 % to 70 % by this integration approach.

Introduction

In recent years, photon-based quantum technologies have made great progress in various fields,¹ such as deep space optical communication (DSOC) using photons,^{2,3} quantum computation,⁴ on-chip photonic circuits,^{5,6} or quantum key distribution (QKD).^{7,8} Such applications require special components such as single-photon emitters (e.g., NV centers in diamond,⁹ 2D materials,¹⁰ or quantum dots¹¹), spin-photon interfaces,¹² and detectors. For the latter, superconducting (nanowire) single-photon detectors (SNSPDs)^{13–19} have prevailed over other potential candidates such as transition edge sensors (TES)²⁰ or single-photon avalanche diodes (SPADs).²¹ In particular, SNSPDs outperform the other systems by their excellent timing resolution in the range of a few ps²² combined with their high system detection efficiency in the visible to near-infrared²³ when integrated into a resonator structure. Furthermore, first detectors have also been tested in the ultra-violet range.²⁴ However, since the thickness of these detectors is typically in the range of a few nm,²⁵ the structural properties at the interface between the detector and substrate are very demanding. Moreover, their detection efficiency strongly depends on the resonator in which they are integrated. For this purpose, multi-layer structures (e.g. distributed Bragg reflectors (DBR)²⁶ or broadband resonators²³) can be used to increase absorption and thus system efficiency. To ensure a clean surface, the materials used to produce a single-sided resonator (here: aluminum mirror and silicon dioxide spacer) underneath the detector are ideally deposited in the same ultra-high vacuum (UHV) chamber as the superconductor and exhibit a combined RMS roughness of less than 0.25 nm. Beyond applications in resonators for SNSPDs, flat aluminum coatings are used for many purposes such as echelle gratings,²⁷ advanced manufacturing technologies including the aerospace industry²⁸ or applications in integrated circuits.²⁹ Hence, improving the fabrication process of aluminum thin films has the potential to lead to advancements in various fields.

Results

Due to their high sensitivity over a wide wavelength range, broadband resonators are of particular interest. For the fabrication of such broadband resonators a suitable mirror material has to be found that ideally can be deposited in the same UHV chamber as the superconductor while at the same time exhibiting a surface roughness of less than 1 nm. To determine suitable mirror materials, we consider gold and aluminum as two potential candidates and compare them to silicon as a standard semiconductor substrate.

Influence of the deposition rate

Fig. 1(a) shows the measured reflectance spectrum of these three materials as a function of the operating wavelength. The results were obtained using a thin film reflectometer (Filmetrics F20) (see Methods section for more details). The recorded data reveal that silicon is not a suitable material for achieving high detection efficiencies due to its low reflectivity above 400 nm ranging between 0.30 and 0.40. We therefore focus on the two remaining materials. While aluminum has the highest reflectivity between 200 nm and 600 nm, it is surpassed by gold between 600 nm and 1200 nm. At even higher wavelengths, gold and aluminum behave almost identically with a reflectivity over 99%. Hence, a sufficient reflectivity can be achieved by either of the two possible materials. However, sputtering gold³⁰ can cause cross contamination and therefore influences other sputtering processes performed in the same chamber. Consequently, we focus on developing a sputter deposition process for high-quality aluminum coatings that combines high reflectivity with low surface roughness. Throughout this work a 525 μm thick Si-wafer with a 127 nm thick thermally grown SiO_2 layer on top was used as a substrate material. For these substrates, the RMS surface roughness was determined to be 0.25 nm, which is close to the resolution limit of the atomic force microscope (AFM).

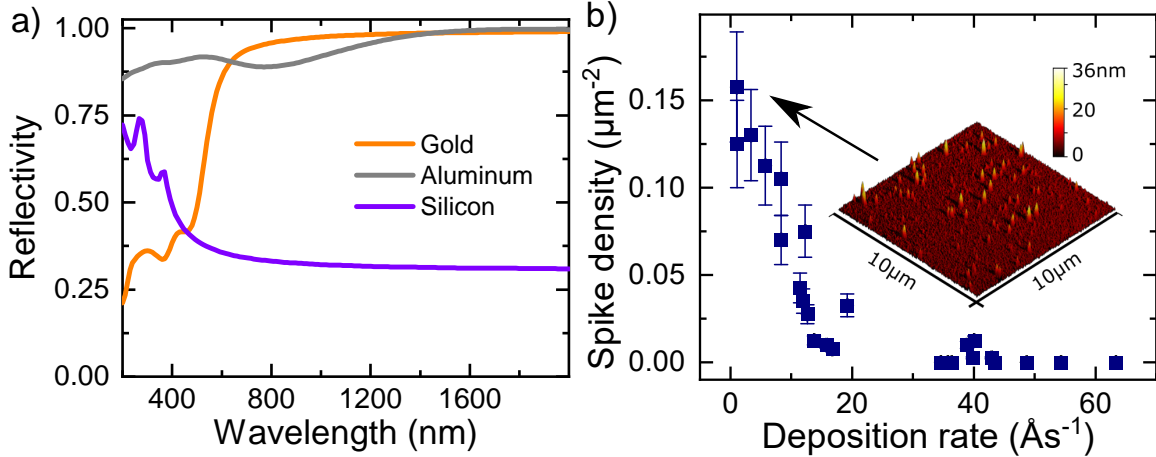


Figure 1. Reflectivity and spike density of potential substrate materials. (a) Measurement of the reflectivity of Au, Al, and Si as a function of the wavelength. While aluminum has the highest reflectivity between 200 nm and 600 nm, it is surpassed by gold between 600 nm and 1200 nm. At even higher wavelengths, gold and aluminum behave almost identically with a reflectivity over 99%. Only the silicon wafer exhibits a significantly lower reflectivity at wavelengths above 400 nm. (b) Spike density as a function of the deposition rate for sputtered aluminum films, as determined from AFM surface topography scans. The inset shows an AFM image for a sample with a high spike density sputtered at a rate of 1 \AA s^{-1} . The error bars spike density represent the standard deviation from multiple AFM scans on a sample.

We start the film optimization by investigating the large peaks present in the deposited material, hereafter referred to as spikes. The inset of Fig. 1(b) shows a typical atomic force microscope (AFM) image for a 50 nm thick Al film deposited by DC magnetron sputtering with a rate of 1 \AA s^{-1} . A detailed description of the acquisition of the AFM images is given in the Methods section. The scan has a size of 10 μm \times 10 μm corresponding to the typical area covered by a superconducting detector. Here, individual spikes can be clearly identified with a maximum height of 36 nm. The spikes are defined as areas that are more than 10 nm above the mean height level of the surface. The spikes are likely caused by residuals of oxygen or water in the atmosphere of the sputtering chamber during deposition^{31,32} or cross-contamination. Fig. 1(b) shows the

measured spike density as a function of deposition rate for various aluminum films. Here, the rate was tuned by various parameters such as the applied power, the distance between the target and substrate holder or the argon sputtering pressure. The data reveal that the spike density decreases with an increased deposition rate up to around 50 \AA s^{-1} . At even higher deposition rates, the spike density is no longer observable. This indicates that the density of spikes depends on the time required for the formation of a monolayer (monolayer formation time). It describes the time required to cover the sample surface by residual substances present in the deposition chamber.³³ At higher deposition rates, the amount of impurities incorporated into the layer decreases, resulting in lower stress and fewer spikes. In addition, we found that cleaning the sputtering target by pre-sputtering prior to deposition is an indispensable step. To investigate this, we produced four mirrors directly one after the other without any cleaning process (sputtering time: 10 s) and measured the corresponding spike density. It decreased from $0.65(2) \mu\text{m}^{-2}$ (S1) over $0.0525(200) \mu\text{m}^{-2}$ (S2) and $0.025(20) \mu\text{m}^{-2}$ (S3) down to $0.02(2) \mu\text{m}^{-2}$ (S4). With increasing sputtering time, contamination is removed from the system and the film quality is improved. This emphasizes the need for a pre-sputtering process prior to sputter deposition, as this in turn leads to less stress and fewer spikes.

Distance to target (mm)	RMS roughness (nm)	Grain size ($10^{-3} \mu\text{m}^2$)	Deposition rate (\AA s^{-1})
40	1.34 ± 0.25	$3.10 \pm 5 \%$	38.9 ± 0.5
80	1.76 ± 0.25	$3.71 \pm 5 \%$	12.6 ± 0.5
120	1.82 ± 0.25	$4.23 \pm 5 \%$	5.8 ± 0.5

Table 1. Influence of the distance between the target and the substrate holder. With decreasing distance, a decreasing surface roughness and grain size is obtained. At the same time, the deposition rate increases significantly as well. The uncertainty of the rate stems from the ratio of the measured deposition rate given by the deposition system and the film thickness determined via X-ray reflectometry (XRR).

In addition, we investigated the influence of the distance between the target and substrate holder on the deposition process for 50 nm thick films as shown in Tab. 1. In particular, we observed an increased deposition rate for decreasing distance. This indicates that a low distance such as 40 mm (system dependent minimum) is preferred as it avoids the formation of spikes (cf. Fig. 1(b)). We note that both the RMS roughness and grain size decreased with decreasing distance as well. To conclude, it is necessary to clean the target from contamination prior to deposition and it is advantageous to use a high deposition rate (for instance by reducing the distance between the substrate holder and target) to achieve high-purity films without spikes.

Impact of the deposition temperature

As a next parameter, we investigated the impact of the substrate temperature during the deposition of 50 nm aluminum films in the range from 20°C to 400°C . The corresponding AFM images covering a size of $3 \mu\text{m} \times 3 \mu\text{m}$ are shown in Fig. 2(a) - Fig. 2(c).

Fig. 2(a) shows a homogeneous film with a maximum height variation of about 16 nm deposited at room temperature using non-optimized fabrication parameters with a power of 200 W, a distance of 80 mm at a pressure of 5×10^{-3} mbar. However, for an increased deposition temperature in Fig. 2(b) and Fig. 2(c), the height variation increases even further up to 71 nm and 121 nm, respectively. Also, the general surface morphology of the presented aluminum films changed significantly as presented in Tab. 2.

Temperature ($^\circ\text{C}$)	RMS roughness (nm)	Grain size ($10^{-3} \mu\text{m}^2$)
20	1.78 ± 0.25	$4.5 \pm 5 \%$
200	9.22 ± 0.25	$62.7 \pm 5 \%$
400	17.21 ± 0.25	$223.5 \pm 5 \%$

Table 2. Obtained roughness and grain size of a 50 nm thick Al film derived from the AFM images shown in Fig. 2(a) - Fig. 2(c). The RMS roughness (from 1.8 nm to 17.2 nm) and grain size (from $4.5 \times 10^{-3} \mu\text{m}^2$ to $223.5 \times 10^{-3} \mu\text{m}^2$) increase significantly with increasing deposition temperature (from 20°C to 400°C).

We observe that the sputtered films exhibit larger grains (average values range from $4.5 \times 10^{-3} \mu\text{m}^2$ to $223.5 \times 10^{-3} \mu\text{m}^2$) and become rougher (from 1.8 nm to 17.2 nm) for an increased deposition temperature (from

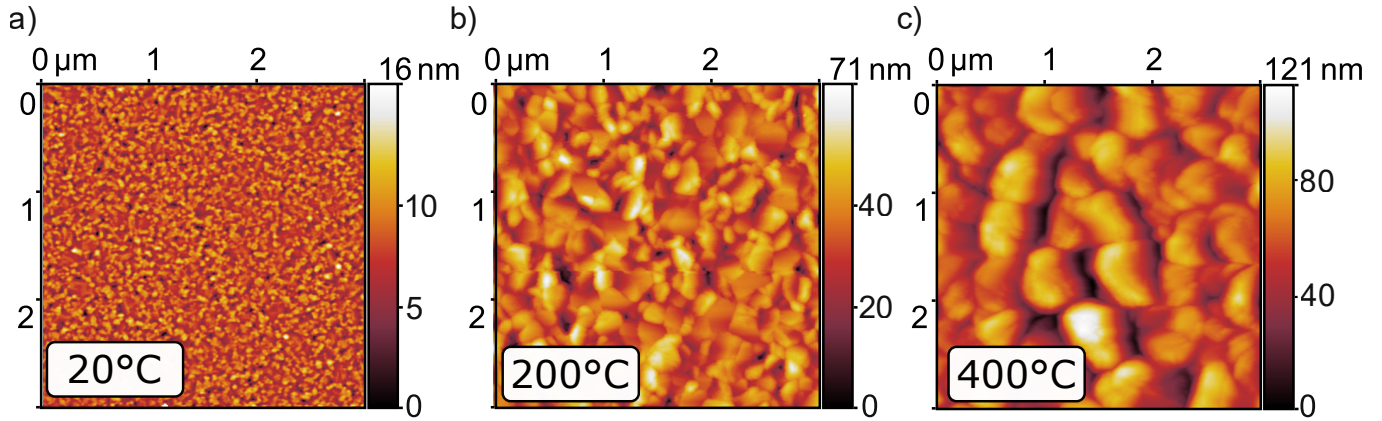


Figure 2. Impact of deposition temperature on the structural properties of aluminum thin films determined by AFM measurements. (a) While the films deposited at room temperature have many small grains, the grain size increases with increasing deposition temperature leading to larger features, as shown in the images (b) at 200 °C and (c) at 400 °C. In addition, the maximum height variation also increases from 16 nm for films deposited at room temperature, over (b) 71 nm at 200 °C up to (c) 121 nm at 400 °C. Hence, a higher deposition temperature leads to larger grains and a higher surface roughness indicating that a room temperature deposition process should be used.

20 °C to 400 °C). We deduce that the grain size and RMS roughness are correlated. In particular, by reducing the grain size the surface roughness is improved. Moreover, the findings indicate that only films sputtered at ambient temperature are suitable for the fabrication of high quality thin films.

Impact of Ar sputtering pressure and applied power

To investigate the impact of the deposition rate in more detail we subsequently analyzed the influence of the argon pressure during the deposition of 75 nm thick aluminum films.

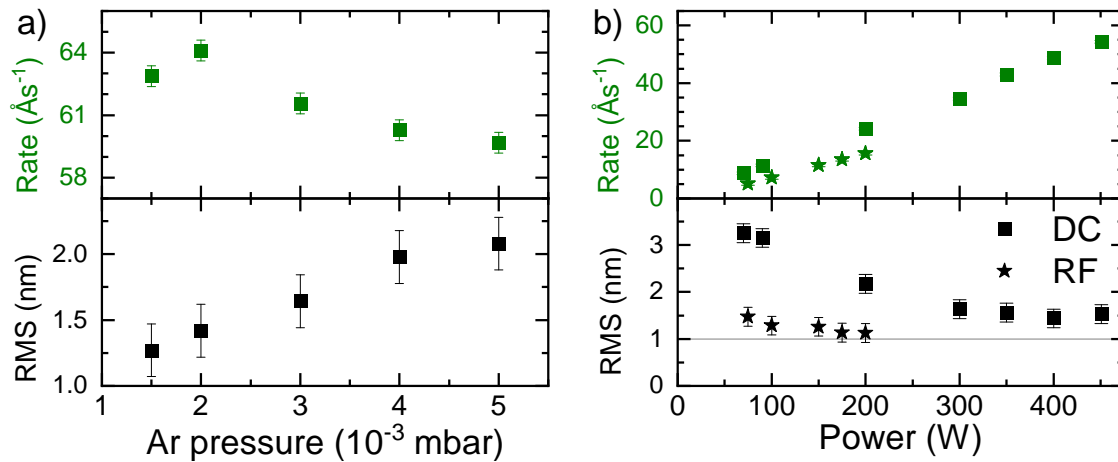


Figure 3. Influence of the deposition rate on the thin film quality. (a) Deposition rate and RMS roughness as a function of argon sputtering gas pressure at a constant power of 450 Watt. Increased rate and improved roughness are observed at reduced pressure. (b) Comparison of deposition rate and surface roughness as a function of applied power for both DC and RF sputtering. For DC sputtering the roughness improves with increasing power at a constant sputtering pressure of 3×10^{-3} mbar. However, RF sputtering allows for even better roughness values at comparatively lower powers.

Fig. 3(a) shows the corresponding RMS roughness and deposition rate as a function of the argon pressure. With an increasing Ar pressure (from 1.5×10^{-3} mbar to 5.0×10^{-3} mbar) the deposition rate decreases (64.2 Å s^{-1} to 59.6 Å s^{-1}) likely due to an increased collision probability between the aluminum and argon atoms and a drop

in DC bias voltage. Simultaneously, an increased roughness (from 1.3 nm to 2.2 nm) can be observed. Note that the applied DC power of 425 W has been selected to avoid the formation of spikes (cf. Fig. 1(b)). Also here, an increased deposition rate resulted in a lower surface roughness and therefore higher quality films. It should be noted, however, that at even lower pressures the plasma is no longer stable. Hence, an argon pressure around 2×10^{-3} mbar is the best parameter for our system. We then investigated the influence of the applied power for both DC and RF magnetron sputtering configuration. Note that one of the main advantages of RF sputtering is that it produces significantly less heat. Fig. 3(b) shows the roughness (bottom) and deposition rate (top) as a function of the applied DC and RF power for an argon pressure of 5×10^{-3} mbar and both power configurations. Here, the data points obtained for DC sputtering are shown as squares and those for RF sputtering as stars. Starting with DC sputtering, we observe that an increased rate is accompanied by a decreased roughness down to 1.5 nm at 425 W (system dependent maximum). However, by using RF sputtering, we were able to improve the roughness even further, from 1.47 nm at 75 W to 1.12 nm at 200 W (system dependent maximum for RF sputtering). We attribute the observed improvement in surface roughness to the reduced heating of the substrate by the RF sputtering process. This is in good agreement with the results from Fig. 2, which showed a direct correlation between the deposition temperature and measured film roughness. Therefore, to achieve the best possible surface roughness, it is advantageous to use an argon pressure in the range of 2×10^{-3} mbar in combination with the RF magnetron sputtering configuration at an applied power of 200 W.

Impact of the aluminum layer thickness on the thin film quality

Finally, we produced and analyzed aluminum films with varying layer thicknesses using the previously optimized fabrication parameters. The corresponding results in Fig. 4(a) show the measured reflectivity at a wavelength of 780 nm, grain size and RMS roughness as a function of the sputtered aluminum thickness. For a thickness above 50 nm, the obtained data reveals a saturating reflectivity at 85 %. Moreover, with an increasing film thickness, both roughness and grain size, plotted on a semi-logarithmic scale, increase significantly. This indicates that small film thicknesses are preferable for ultra-flat coatings. In particular, for film thicknesses below 50 nm we obtain a roughness of less than 1 nm as well as a grain size of less than $2 \times 10^{-3} \mu\text{m}^2$ indicating a high film homogeneity. Fig. 4(b) shows a corresponding AFM scan with a low surface roughness and no spikes. If we now combine the previously determined results, we conclude that an aluminum layer thickness of 50 nm should be used. It allows us to fabricate smooth thin films with a grain size of less than $2 \times 10^{-3} \mu\text{m}^2$ accompanied by a low surface roughness (< 1 nm RMS) and saturating reflectivity.

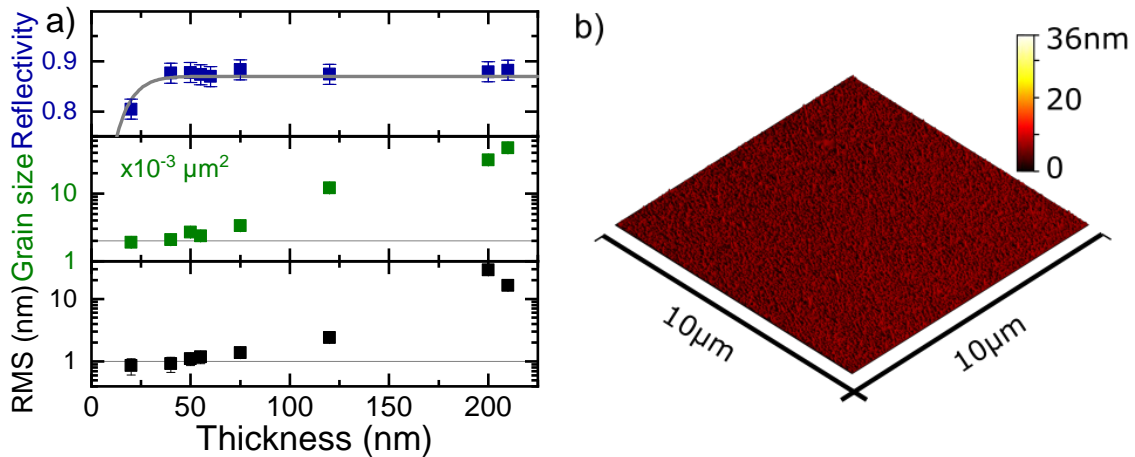


Figure 4. Influence of film thickness on the surface quality for coatings produced by the optimized manufacturing process. (a) Dependence of surface roughness, grain size and reflectivity on the aluminum thickness, plotted on a semi-logarithmic scales. With increasing film thickness, both roughness and grain size increase, while the reflectivity saturates with increasing thickness. (b) AFM image of a sample prepared by the optimized fabrication method shows a low surface roughness and no spikes.

Superconducting detectors on aluminum mirrors

To confirm the high quality of the optimized aluminum mirrors, we benchmark superconducting nanowire single-photon detectors (SNSPDs) fabricated on an aluminum-silica one-sided resonator. The multi-layer heterostructure consists of an aluminum mirror buried below a silicon dioxide spacer on top of which the NbTiN detector is fabricated. These detectors consist of a meandering nanowire with a typical wire width around 100 nm, a thickness below 10 nm and are cooled down well below the superconductors critical temperature. When now a current is applied near the so-called critical current, the energy of a single photon is sufficient to destroy the superconducting state and a normal conducting barrier is formed. The voltage pulse generated by this process can then be amplified and measured.^{13,34}

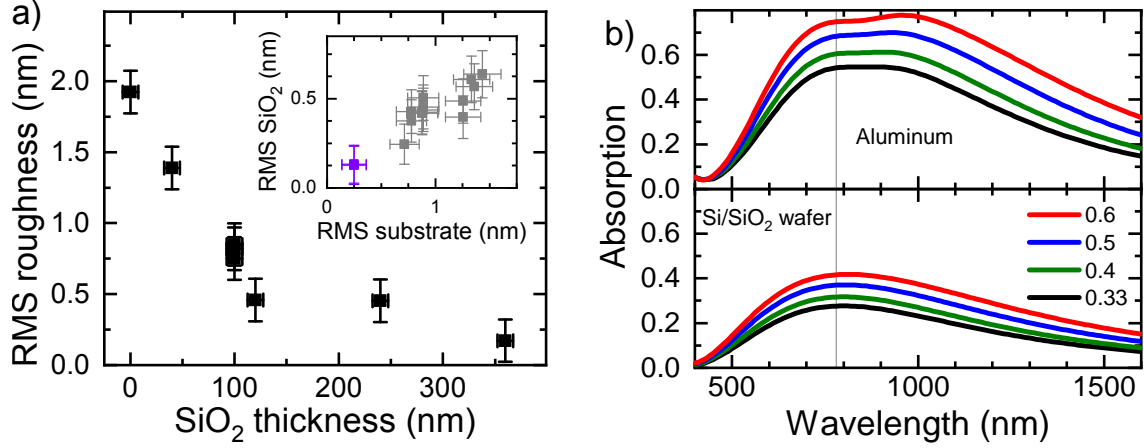


Figure 5. Integration of superconducting single-photon detectors into a single-sided resonator consisting of an aluminum mirror and a SiO₂ spacer. (a) The surface roughness can be improved by introducing a SiO₂ top layer. For a film thickness of 120 nm, the roughness decreased from 1.92 nm down to 0.46 nm. The inset shows the improvement of films with different roughness before and after the deposition of 120 nm SiO₂. (b) Simulated absorption of detectors with varied fill factor from 0.33 (black) to 0.6 (red) on the semi-sided aluminum resonator with a dielectric, 120 nm thick SiO₂ spacer on top of a Si/SiO₂ substrate (top panel). Simulated detector absorbance on bare silicon wafer with 127 nm thermally grown SiO₂ only (bottom panel). The reference line marks the operating wavelength of 780 nm used in this work. The data reveal an increased absorption probability for the semi-sided aluminum resonator independent of the wavelength. The top panel reveals a broad spectral range of high absorption in the range from 750 nm to 1000 nm for a SiO₂ thickness optimized for operation at 780 nm.

The roughness of the fabricated multi-layer structure consisting of the aluminum film and a silicon dioxide layer with a thickness in the range from 0 nm to 360 nm is shown in Fig. 5(a). For this study we did not use the fully-optimized parameters in order to analyze the impact of the SiO₂ thickness in more detail. For an initial roughness of 1.92 nm we observe a strong decrease down to 0.46 nm for a silica layer thickness of approximately 120 nm. For even thicker silica films only small improvements can be seen. Note that the initial roughness of the wafer itself is around 0.25 nm. The inset of Fig. 5(a) depicts the improvement of films with different roughness before and after the deposition of 120 nm SiO₂. Especially the aluminum mirrors (grey) show that the roughness improves by a factor of two even for films that already had an initial roughness below 1 nm. Hence, by combining the optimized deposition processes for aluminum and silicon dioxide we are able to fabricate a broadband resonator with an RMS roughness comparable to a commercially available silicon dioxide-on-silicon wafer around 0.25 nm. Fig. 5(b) presents the simulated absorption as a function of the operating wavelength. In the bottom panel, a silicon wafer with a 127 nm thick thermally grown SiO₂ layer was used. Here, the absorption increases with the fill factor and shows a fill factor-dependent maximum at a wavelength of 780 nm corresponding to the design wavelength of the optical stack. The data reveal a maximum absorption of 27.6% for a fill factor of 0.33 and an absorption of 41.6% for a fill factor of 0.6. In the top panel, the results for a semi-sided resonator of 120 nm SiO₂ on top of 50 nm Al are shown. The absorption probability increases with an increasing fill factor as well and is almost doubled compared to the Si/SiO₂ wafer. Here, absorption values of 54.2% (fill factor 0.33) and 74.8% (fill factor 0.6) were determined. The SiO₂ thickness was chosen according to the simulation results

and formed a $\lambda/4$ resonator for a refractive index $n = 1.46$ of SiO_2 .³⁵ Furthermore, note the broad spectral range of high absorption from 750 nm to 1000 nm. To conclude, the obtained results show that the aluminum resonator improves the absorption probability by forming a broad optical resonator.

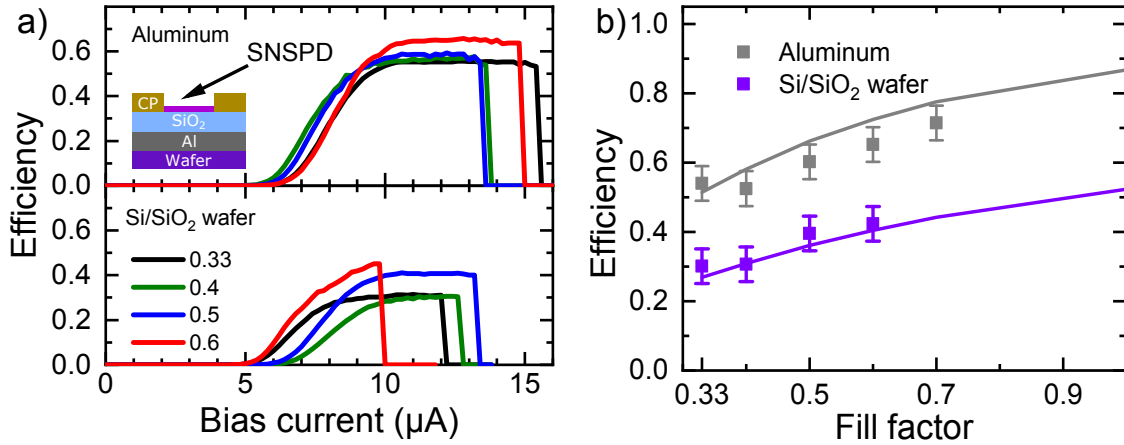


Figure 6. Integration of superconducting single-photon detectors into a single-sided resonator consisting of an aluminum mirror and a SiO_2 spacer. (a) Detection efficiency of superconducting detectors as a function of the applied bias current at a wavelength of 780 nm. The data shows detectors with fill factors 0.33 (black), 0.4 (green), 0.5 (blue), and 0.6 (red). The bottom panel shows results for detectors fabricated directly on top of the Si/SiO_2 wafer, while the top panel shows the results for the aluminum semi-sided resonator. The detection efficiency increases with increasing current until it starts to saturate from around 10 μA indicating an internal quantum efficiency of one. The typical switching current ranges between 12 μA to 15 μA with one outlier at 10 μA for a fill factor of 0.6. While efficiencies up to 40% were achieved on top of the wafer, the bottom resonator allowed to improve the efficiency up to 70%. The inset shows a sketch of the multi-layer structure used for the semi-sided resonator including the wafer, the aluminum mirror, the SiO_2 spacer, the superconducting detector (SNSPD) and the contact pads (CP) used for electrical contacting the device. (b) Summary of the measured detection efficiencies as a function of the fill factor at a wavelength of 780 nm. In agreement with simulations, the aluminum mirror improves the absorption and therefore detection efficiency significantly compared to a silicon dioxide-on-silicon wafer. The solid lines correspond to the simulation results shown before at a fixed wavelength of 780 nm.

Finally, Fig. 6 shows the measured detection efficiencies of detectors fabricated on top of a silicon dioxide-on-silicon wafer and on top of a silicon dioxide-on-aluminum bottom resonator. Fig. 6(a) presents the measured detection efficiency for 6 nm thick meandering NbTiN detectors with a buried aluminum mirror in the top panel and without a mirror in the bottom panel as a function of the applied bias current. Here, the fill factor was varied between 0.33 (black) and 0.6 (red). The devices were measured at 4.5 K and operated at a wavelength of 780 nm. The inset in the top panel shows a sketch of the multi-layer structure used. Here, the detector (SNSPD) is embedded in a semi-sided resonator structure composed of the silicon wafer, the aluminum mirror, and the SiO_2 spacer. The titanium/gold contact pads (CP) are used for electrically contacting the device. Both presented data sets show an increasing detection efficiency with an increasing bias current from 5 μA to 10 μA , where the measured efficiency start to saturate. This behavior is an indication of an internal quantum efficiency of one.³⁶ This saturation persists until the switching current is exceeded, in the range between 12 μA to 15 μA with one outlier at 10 μA for a fill factor of 0.6. The higher switching current of the detectors on the aluminum mirror indicate that the detector fabrication worked slightly better for this sample. These superconducting films on top of the Si/SiO_2 wafer (on the Al/SiO_2 mirror) had a critical temperature of 8.9 K (8.4 K), a sheet resistance of 630 Ω (590 Ω) measured at 20 K,³⁷ and a residual resistance ratio³⁸ of 0.88 (0.86). Note that a further increase in sheet resistance and decrease in critical temperature have been found to enhance the sensitivity to single photons,³⁶ particularly for longer wavelengths.³⁹ In addition, the data reveal an efficiency up to around 40% on top of the silicon dioxide-on-silicon wafer with a SiO_2 thickness of 127 nm. For the same detectors fabricated on top of the Al/SiO_2 semi-sided resonator, efficiencies up to 70% were measured. Here, an optimized aluminum mirror with a thickness of 50 nm buried underneath a 120 nm thick SiO_2 layer was used. Fig. 6(b) depicts a summary of the efficiency as a function of the fill factor. A significant improvement of the detection

efficiency is observed, in FDTD simulations of the absorption (solid lines), which represent the upper limit of the theoretically achievable detection efficiency corresponding to the simulation results shown in Fig. 5(b). More detailed information about the FDTD simulations can be found in the Methods section. To conclude, we were able to boost the efficiency from around 40 % up to 70 % by only using a broadband semi-sided resonator as an SNSPD substrate.

Conclusion

In this study, we investigated the growth conditions for ultra-thin aluminum films that can be used for various applications ranging from the aerospace industry to quantum devices. To obtain high-quality films, we developed the sputtering process shown in Tab. 3.

Parameter	Optimized value	Parameter	Optimized value
Temperature	20 °C	Distance	40 mm
Thickness	50 nm	Ar pressure	2×10^{-3} mbar
Configuration	RF	Power	200 W

Table 3. Overview of the optimized parameter set used to sputter the high quality aluminum films.

It should be noted, however, that these optimized values may differ slightly for different sputtering systems. By tuning parameters such as the deposition rate, temperature or power, we were able to produce 50 nm Al thin films with a roughness less than 1 nm and high reflectivity. We also found that the roughness of the films is directly linked to the grain size and, thus, were able to improve the surface roughness by reducing the grain size. Subsequently, we added a SiO₂ layer and fabricated a superconducting nanowire single-photon detector on top. This procedure allowed us to reduce the roughness down to 0.25 nm, which is similar to the roughness of a silicon wafer. In agreement with FDTD simulations, we were able to boost the detection efficiency at an operation wavelength of 780 nm from 40 % up to 70 % by only using a single-sided resonator underneath the device. Furthermore, note that it is possible to tune the design wavelength of the resonator by adjusting the SiO₂ thickness (cp. Fig. 5(b)). For even longer wavelengths, thicker dielectric layers are required, which simultaneously allow to further reduce the overall surface roughness.

Methods

DC and RF magnetron sputtering

For the deposition of our thin film materials, including Al, we use a BESTEC UHV Sputter-Deposition-System, containing multiple 2 inch and 3 inch sputter targets with DC and RF power supplies. To produce contaminant-free films we pump the system down to a base pressure $<1 \times 10^{-8}$ mbar. Subsequently, a sputtering atmosphere of pure Ar gas and constant pressure is realized by a down-stream pressure control system. Next, the Ar plasma is ignited by either a DC or RF power supply, after which the deposition rate is determined via a thickness sensor giving full control of the film thickness. Beyond that, the substrate is continuously rotated during the sputter process to obtain a homogeneous aluminum film.

Film characterization and analysis

To analyze the reflectivity of the deposited films, a reflectometer (Filmetrics F20) was used. The reflectometer covers a broad spectral range from 200 nm to 1000 nm. The beam was focused on the sample surface. The reflected light was then analyzed by a spectrometer, which can resolve intensities of light with a spectral accuracy below 1 nm. The surface roughness was measured with the help of an atomic force microscope (AFM, Asylum Research MFP-3D) operated in tapping mode and an AC240TS-R3 tip. The AFM had a resolution limit of around 0.25 nm in roughness. The AFM scans were analyzed using the open-source software Gwyddion. Here, the RMS surface roughness is defined as $R_{rms} = (N^{-1} \sum_{i=1}^N (z_i - \bar{z})^2)^{1/2}$ with the number of scan points N and their respective height z_i . Spikes were defined by introducing a height threshold (10 nm above the mean level). Lastly, the mentioned grains are defined and measured via the so-called watershed segmentation algorithm⁴⁰ allowing to analyze the structural properties.

Detector fabrication and characterization

After the deposition of the different materials including Al, SiO₂ and NbTiN, we pattern the devices by electron beam lithography (EBL) using a negative-tone eBeam resist. After development, the design is transferred into the NbTiN layer via a dry etching process in a reactive ion etching (RIE) system. Subsequently, the geometry of the electrical contact pads is patterned using optical lithography and subsequently developed. Finally, thin layers of titanium and gold are evaporated. Afterward, a liftoff process is used to remove excessive material. The detectors were characterized in a cryogenic probe station from Janis operated at 4.5 K sample surface temperature. Here, a calibrated parallel beam is used that allows flood illumination and fast characterization of multiple devices.¹⁹ By broadening the beam to a diameter of about 500 μm using lensed optics, a homogeneous beam spot is generated with a reduced incident photon flux per 10 μm \times 10 μm by means of geometric attenuation. After calibrating the ratio of the light impinging on the detector area to the overall incident photon flux by performing a 2D scan over the sample with the detector (typically 5 mm \times 5 mm) in the center, the detection efficiency can be determined. Thus, positioning the laser with submicron precision can be avoided as small deviations in position do not correspond to significant changes in the incident photon flux on the active detector. Subsequently, the measured photon count rate is compared with the number of incoming photons on the detector area considering the previously mentioned geometric attenuation. Finally, the measured optical properties are compared to finite-difference time-domain (FDTD) simulations using the commercially available software Lumerical (Ansys). Here, the optical response of an SNSPD is approximated by a single nanowire section embedded in an optical resonator with the appropriate optical material constants and periodic boundary conditions. This is possible since the detector geometry is symmetric in the active area of the detector, which reduces simulation times.

Author contributions statement

R.F. conceived the experiments and drafted manuscript. R.F., and C.S. conducted the experiments and analysed the results. R.F., C.S. and L.Z. fabricated samples. M.M. supported the thin film deposition processes and growth optimization. M.A. and R.G. led the research work related to thin film deposition technology. J.F. and K.M. led the research projects. All authors discussed the results and reviewed the manuscript.

Competing interests

The authors declare no competing interests.

Funding

We gratefully acknowledge the German Federal Ministry of Education and Research via the funding program Photonics Research Germany (contract number 13N14846), via the funding program quantum technologies - from basic research to market (contract numbers 16K1SQ033, 13N15855, 13N15982, 13N16214 and 13N15760), and via the projects Q.com (contract number 16KIS0110) and MARQUAND (contract number BN105022), as well as the Deutsche Forschungsgemeinschaft (DFG, German Research Foundation) under Germany's Excellence Strategy – EXC-2111 – 390814868. This research is part of the Munich Quantum Valley, which is supported by the Bavarian state government with funds from the Hightech Agenda Bayern Plus.

REFERENCES

- [1] Kimble, H., “The quantum internet,” *Nature* **453**, 1023–1030 (2008).
- [2] Caloz, M., Korzh, B., Ramirez, E., Schönenberger, C., Warburton, R. J., Zbinden, H., Shaw, M. D., and Bussières, F., “Intrinsically-limited timing jitter in molybdenum silicide superconducting nanowire single-photon detectors,” *Journal of Applied Physics* **126**(16), 164501 (2019).
- [3] Ivanov, H. and Leitgeb, E., “Characteristics of ultra-long deep space fso downlinks using special detector technologies like snsps,” in [2020 22nd International Conference on Transparent Optical Networks (ICTON)], 1–4, IEEE (2020).
- [4] Singh, J. and Singh, M., “Evolution in quantum computing,” in [2016 International Conference System Modeling & Advancement in Research Trends (SMART)], 267–270, IEEE (2016).

- [5] Wang, J., Sciarrino, F., Laing, A., and Thompson, M. G., “Integrated photonic quantum technologies,” *Nature Photonics* **14**(5), 273–284 (2020).
- [6] Terhaar, R., Rödiger, J., Häußler, M., Wahl, M., Gehring, H., Wolff, M. A., Beutel, F., Hartmann, W., Walter, N., Hanke, J., et al., “Ultrafast quantum key distribution using fully parallelized quantum channels,” *arXiv preprint arXiv:2207.07345* (2022).
- [7] Bennett, C. H. and Brassard, G., “Proceedings of the IEEE international conference on computers, systems and signal processing,” (1984).
- [8] Shibata, H., Honjo, T., and Shimizu, K., “Quantum key distribution over a 72 db channel loss using ultralow dark count superconducting single-photon detectors,” *Optics letters* **39**(17), 5078–5081 (2014).
- [9] Kurtsiefer, C., Mayer, S., Zarda, P., and Weinfurter, H., “Stable solid-state source of single photons,” *Physical review letters* **85**(2), 290 (2000).
- [10] Tran, T. T., Elbadawi, C., Totonjian, D., Lobo, C. J., Grosso, G., Moon, H., Englund, D. R., Ford, M. J., Aharonovich, I., and Toth, M., “Robust multicolor single photon emission from point defects in hexagonal boron nitride,” *ACS nano* **10**(8), 7331–7338 (2016).
- [11] Senellart, P., Solomon, G., and White, A., “High-performance semiconductor quantum-dot single-photon sources,” *Nature nanotechnology* **12**(11), 1026–1039 (2017).
- [12] Atatüre, M., Englund, D., Vamivakas, N., Lee, S.-Y., and Wrachtrup, J., “Material platforms for spin-based photonic quantum technologies,” *Nature Reviews Materials* **3**(5), 38–51 (2018).
- [13] Gol’tsman, G., Okunev, O., Chulkova, G., Lipatov, A., Dzardanov, A., Smirnov, K., Semenov, A., Voronov, B., Williams, C., and Sobolewski, R., “Fabrication and properties of an ultrafast nbn hot-electron single-photon detector,” *IEEE Transactions on applied superconductivity* **11**(1), 574–577 (2001).
- [14] Reithmaier, G., Senf, J., Lichtmanecker, S., Reichert, T., Flassig, F., Voss, A., Gross, R., and Finley, J., “Optimisation of nbn thin films on gaas substrates for in-situ single photon detection in structured photonic devices,” *Journal of Applied Physics* **113**(14), 143507 (2013).
- [15] Reithmaier, G., Lichtmanecker, S., Reichert, T., Hasch, P., Müller, K., Bichler, M., Gross, R., and Finley, J. J., “On-chip time resolved detection of quantum dot emission using integrated superconducting single photon detectors,” *Scientific reports* **3**(1), 1–6 (2013).
- [16] Reithmaier, G., Kaniber, M., Flassig, F., Lichtmanecker, S., Müller, K., Andrejew, A., Vuckovic, J., Gross, R., and Finley, J., “On-chip generation, routing, and detection of resonance fluorescence,” *Nano letters* **15**(8), 5208–5213 (2015).
- [17] Redaelli, L., Bulgarini, G., Dobrovolskiy, S., Dorenbos, S. N., Zwiller, V., Monroy, E., and Gérard, J.-M., “Design of broadband high-efficiency superconducting-nanowire single photon detectors,” *Superconductor Science and Technology* **29**(6), 065016 (2016).
- [18] Flassig, F., Flaschmann, R., Kainz, T., Ernst, S., Strothauer, S., Schmid, C., Zugliani, L., Müller, K., and Finley, J. J., “Automated, deep reactive ion etching free fiber coupling to nanophotonic devices,” in [*Quantum Sensing and Nano Electronics and Photonics XVIII*], **12009**, 102–110, SPIE (2022).
- [19] Flaschmann, R., Zugliani, L., Schmid, C., Spedicato, S., Strothauer, S., Wietschorke, F., Flassig, F., Finley, J. J., and Müller, K., “The dependence of timing jitter of superconducting nanowire single-photon detectors on the multi-layer sample design and slew rate,” *Nanoscale* **15**, 1086–1091 (2023).
- [20] Ullom, J. N. and Bennett, D. A., “Review of superconducting transition-edge sensors for x-ray and gamma-ray spectroscopy,” *Superconductor Science and Technology* **28**(8), 084003 (2015).
- [21] Nix, F. C., “Photo-conductivity,” *Reviews of Modern Physics* **4**(4), 723 (1932).
- [22] Korzh, B., Zhao, Q.-Y., Allmaras, J. P., Frasca, S., Autry, T. M., Bersin, E. A., Beyer, A. D., Briggs, R. M., Bumble, B., Colangelo, M., et al., “Demonstration of sub-3 ps temporal resolution with a superconducting nanowire single-photon detector,” *Nature Photonics* **14**(4), 250–255 (2020).
- [23] Reddy, D. V., Nerem, R. R., Nam, S. W., Mirin, R. P., and Verma, V. B., “Superconducting nanowire single-photon detectors with 98% system detection efficiency at 1550 nm,” *Optica* **7**(12), 1649–1653 (2020).
- [24] Wollman, E. E., Verma, V. B., Beyer, A. D., Briggs, R. M., Korzh, B., Allmaras, J. P., Marsili, F., Lita, A. E., Mirin, R., Nam, S., et al., “Uv superconducting nanowire single-photon detectors with high efficiency, low noise, and 4 k operating temperature,” *Optics express* **25**(22), 26792–26801 (2017).

- [25] Wolff, M. A., Vogel, S., Splitthoff, L., and Schuck, C., “Superconducting nanowire single-photon detectors integrated with tantalum pentoxide waveguides,” *Scientific Reports* **10**(1), 1–9 (2020).
- [26] Zhang, W., You, L., Li, H., Huang, J., Lv, C., Zhang, L., Liu, X., Wu, J., Wang, Z., and Xie, X., “Nbn superconducting nanowire single photon detector with efficiency over 90% at 1550 nm wavelength operational at compact cryocooler temperature,” *Science China Physics, Mechanics & Astronomy* **60**(12), 1–10 (2017).
- [27] Li, Z., Gao, J., Yang, H., Wang, T., and Wang, X., “Roughness reduction of large-area high-quality thick al films for echelle gratings by multi-step deposition method,” *Optics express* **23**(18), 23738–23747 (2015).
- [28] Xie, G., Bai, H., Miao, G., Feng, G., Yang, J., He, Y., Li, X., and Li, Y., “The applications of ultra-thin nanofilm for aerospace advanced manufacturing technology,” *Nanomaterials* **11**(12), 3282 (2021).
- [29] Roberts, S. and Dobson, P., “The microstructure of aluminium thin films on amorphous sio₂,” *Thin solid films* **135**(1), 137–148 (1986).
- [30] Xin, Z., Xiao-Hui, S., and Dian-Lin, Z., “Thickness dependence of grain size and surface roughness for dc magnetron sputtered au films,” *Chinese Physics B* **19**, 086802 (aug 2010).
- [31] Verkerk, M. and Brankaert, W., “Effects of water on the growth of aluminium films deposited by vacuum evaporation,” *Thin Solid Films* **139**(1), 77–88 (1986).
- [32] Chang, C. and Vook, R., “Topography and microstructure of al films formed under various deposition conditions,” *Journal of Vacuum Science & Technology A: Vacuum, Surfaces, and Films* **9**(3), 559–562 (1991).
- [33] Quijada, M. A., Del Hoyo, J. G., Gray, E., Richardson, J. G., Howe, A., de Marcos, L. R., and Sheikh, D. A., “Influence of evaporation rate and chamber pressure on the fuv reflectance and physical characteristics of aluminum films,” in [*UV/Optical/IR Space Telescopes and Instruments: Innovative Technologies and Concepts X*], **11819**, 153–162, SPIE (2021).
- [34] Natarjan, C. M., Tanner, M. G., and Hadfield, R. H., “Superconducting nanowire single-photon detectors: physics and applications,” *Superconductor Science and Technology* **25**, 063001 (2012).
- [35] Borowicz, P., Latek, M., Rządkiwicz, W., Laszcz, A., Czerwinski, A., and Ratajczak, J., “Deep-ultraviolet raman investigation of silicon oxide: thin film on silicon substrate versus bulk material,” *Advances in Natural Sciences: Nanoscience and Nanotechnology* **3**(4), 045003 (2012).
- [36] Zolotov, P., Svyatodukh, S., Divochiy, A., Seleznev, V., and Goltsman, G., “High-resistivity niobium nitride films for unity-efficiency smpds at telecom wavelengths and beyond,” *arXiv preprint arXiv:2301.00400* (2023).
- [37] Smits, F., “Measurement of sheet resistivities with the four-point probe,” *Bell System Technical Journal* **37**(3), 711–718 (1958).
- [38] Bartolf, H., “Fluctuation mechanisms in superconductors,” in [*Fluctuation Mechanisms in Superconductors*], 181–184, Springer (2016).
- [39] Semenov, A., Engel, A., Hübers, H.-W., Il’in, K., and Siegel, M., “Spectral cut-off in the efficiency of the resistive state formation caused by absorption of a single-photon in current-carrying superconducting nano-strips,” *The European Physical Journal B-Condensed Matter and Complex Systems* **47**(4), 495–501 (2005).
- [40] Chuang, H.-S. and Lin, C.-H., “Automated grain sizing using mark-based watershed algorithm,” in [*2012 IEEE International Geoscience and Remote Sensing Symposium*], 2332–2335, IEEE (2012).